

---

# ALMA observations of the dense and shocked gas in the nuclear region of NGC 4038 (Antennae galaxies)

Junko UEDA<sup>1,2,\*</sup>, Yoshimasa WATANABE<sup>3</sup>, Daisuke IONO<sup>2,4</sup>, David J. WILNER<sup>1</sup>, Giovanni G. FAZIO<sup>1</sup>, Satoshi OHASHI<sup>2,5</sup>, Ryohei KAWABE<sup>2,4,5</sup>, Toshiki SAITO<sup>2,5</sup>, Shinya KOMUGI<sup>6</sup>

<sup>1</sup>Harvard-Smithsonian Center for Astrophysics, 60 Garden Street, Cambridge, MA 02138, USA

<sup>2</sup>National Astronomical Observatory of Japan, 2-21-1 Osawa, Mitaka, Tokyo, 181-8588, Japan

<sup>3</sup>Department of Physics, The University of Tokyo, 7-3-1 Hongo, Bunkyo-ku, Tokyo, 113-0033, Japan

<sup>4</sup>The Graduate University for Advanced Studies (SOKENDAI), 2-21-1 Osawa, Mitaka, Tokyo 181-8588, Japan

<sup>5</sup>Department of Astronomy, The University of Tokyo, 7-3-1 Hongo, Bunkyo-ku, Tokyo 133-0033, Japan

<sup>6</sup>Division of Liberal Arts, Kogakuin University, 2665-1, Hachioji, Tokyo 192-0015, Japan

\*E-mail: junko.ueda@cfa.harvard.edu

Received (reception date); Accepted (acceptation date)

## Abstract

We present 1'' (<100 pc) resolution maps of millimeter emission from five molecules—CN, HCN, HCO<sup>+</sup>, CH<sub>3</sub>OH, and HNCO—obtained towards NGC 4038, which is the northern galaxy of the mid-stage merger, Antennae galaxies, with the Atacama Large Millimeter/submillimeter Array. Three molecules (CN, CH<sub>3</sub>OH, and HNCO) were detected for the first time in the nuclear region of NGC 4038. High-resolution mapping reveals a systematic difference in distributions of different molecular species and continuum emission. Active star forming regions identified by the 3 mm and 850 μm continuum emission are offset from the gas-rich region associated with the HCN (1–0) and CO (3–2) peaks. The CN (1–0)/HCN (1–0) line ratios are enhanced (CN/HCN  $\simeq$  0.8–1.2) in the star forming regions, suggesting that the regions are photon dominated. The large molecular gas mass ( $10^8 M_{\odot}$ ) within a 0''.6 (~60 pc) radius of the CO (3–2) peak and a high dense gas fraction (>20 %) suggested by the HCN (1–0)/CO (3–2) line ratio may signify a future burst of intense star formation there. The shocked gas traced in the CH<sub>3</sub>OH and HNCO emission indicates sub-kpc scale molecular shocks. We suggest that the molecular shocks may be driven by collisions between inflowing gas and the central massive molecular complex.

**Key words:** Galaxies: individual (NGC 4038) — Galaxies: interactions — Radio lines: galaxies

---

## 1 Introduction

Dynamical interactions and mergers of two comparable mass gas-rich galaxies can result in galaxies bright in IR luminosity (e.g., ultra/luminous infrared galaxies (U/LIRGs)). While

recent numerical studies have shown that disk wide starbursts produced by mass fragmentation and turbulent motion across the disk can contribute to the overall star formation activity in colliding systems (Teyssier et al. 2010), it has been long pre-

dicted that the ubiquitous presence of large-scale gas inflows leads to central gas accumulation and subsequent nuclear starburst activity (Mihos & Hernquist 1996). The inflowing gas could collide with gas component associated with the nuclear disk/ring, causing molecular shocks. Although evidence for gas inflows on galactic scales has been discovered in neutral gas (e.g., Hibbard & van Gorkom 1996; Iono et al. 2005) and ionized gas (e.g., Rampazzo et al. 2005; Kewley et al. 2010), there have been few observational confirmations of gas inflows on  $\leq 1$  kpc scale.

The Antennae galaxies (NGC 4038/9) are the nearest (22 Mpc ( $1'' = 107$  pc); Schweizer et al. 2008) mid-stage merger. It is well known that active star formation is ongoing in the off-nuclear region, called the “overlap region” (e.g., Wang et al. 2004), and that the two nuclear regions have lower star formation rates (SFRs) than the overlap region. The SFR of NGC 4038 is estimated to be  $\sim 1 M_{\odot} \text{ yr}^{-1}$  using the Herschel-PACS data (Klaas et al. 2010). The molecular gas mass within the central 1 kpc regions of NGC 4038/9 exceeds that of our Galaxy by a factor of almost 100 (Schulz et al. 2007), revealing high gas concentration into the two nuclei. The extensive amount of molecular gas around the nuclei suggests that this galaxy pair may develop into a ULIRG-like star forming galaxy in the future. The distribution and characteristics of molecular gas in the Antennae galaxies have been investigated using the CO emission (e.g., Wilson et al. 2000; Ueda et al. 2012; Whitmore et al. 2014) and dense gas tracers (i.e., HCN, HCO<sup>+</sup>; Bigiel et al. 2015; Schirm et al. 2016). In previous dense gas observations, the distribution and properties of molecular gas and star formation rates were compared between different regions within the Antennae galaxies. In this study, we focus on the nuclear region of NGC 4038, which is the northern galaxy of the Antennae galaxies, and investigate the distributions of the dense and shocked gas at a 100 pc scale. The purposes of this study are to reveal dusty star forming regions using dense gas tracers and continuum emission, and search for the presence of gas inflows using potential molecular line tracers of shocks (SiO, CH<sub>3</sub>OH, HNC). Although it was previously difficult to observe these shock tracers in NGC 4038 due to a lack of sensitivity, they are now accessible with the sensitivity achievable with the Atacama Large Millimeter/submillimeter Array (ALMA).

## 2 Observations and Archival Data

### 2.1 ALMA Multi-line Observations at Band 3

The multi-line observations of NGC 4038 were carried out using ALMA on July and August, 2014. The number of available 12 m antennas ranged from 31 to 33 depending on the observing run. We used four spectral windows whose frequencies were centered on the lines of SiO (2–1), HCO<sup>+</sup>(1–0), CH<sub>3</sub>OH ( $2_k-1_k$ ), and CN (1–0; 1/2–1/2) redshifted to the ve-

locity of 1638 km s<sup>-1</sup>. Each spectral window was configured with 1.875 GHz bandwidth and 488 kHz frequency resolution. The total frequency coverage is 7.47 GHz (87.78–91.51 GHz, 97.15–99.02 GHz, and 111.56–113.43 GHz). The system temperatures ranged from 40 K to 90 K at the frequencies. The data were obtained using a single pointing (Figure 1 (left)). The primary beam of the 12 m antenna is  $53''-70''$  depending on the frequency of observations. The quasar J1130-1449 was observed for bandpass calibration and the quasar J1215-1731 was observed for phase and amplitude calibration. Absolute flux calibration was performed using Ceres. The uncertainty of absolute flux calibration is 5% in Band 3 according to ALMA Cycle 2 Technical Handbook (Lundgren 2013).

Data calibration and imaging was carried out using the Common Astronomy Software Applications package (CASA; Ver. 4.3.1). We used natural weighting of the visibilities for imaging to obtain the highest sensitivity. The synthesized beam sizes range between  $0.''68$  and  $0.''92$ , and the achieved rms noise levels in the velocity resolution of 10 km s<sup>-1</sup> range between 1.8 mJy beam<sup>-1</sup> and 2.4 mJy beam<sup>-1</sup> (Table 1). We made the 3 mm continuum map using the line free channels. The synthesized beam size of the continuum map is  $0.''95 \times 0.''65$  and the rms noise level is 0.05 mJy beam<sup>-1</sup>.

### 2.2 ALMA CO (3–2) Science Verification Data

We used ALMA CO (3–2) Science Verification (SV) data of the Antennae galaxies. According to instructions in the CASA guide, we applied self-calibration to the calibrated visibility data and made the CO (3–2) map using the CASA (Ver. 4.3.1). The synthesized beam size is  $1.''11 \times 0.''65$  by adopting Briggs weighting of the visibilities (robust = 0.5). The rms noise level at the velocity resolution of 10 km s<sup>-1</sup> is 4.7 mJy beam<sup>-1</sup>. We made the 850  $\mu\text{m}$  continuum map using the line free channels. The synthesized beam size of the continuum map is  $1.''22 \times 0.''73$  by adopting Briggs weighting (robust = 0.5) and the rms noise level is 0.47 mJy beam<sup>-1</sup>.

## 3 Results of the new observations

The new data contain detections of five molecules (CN, HCN, HCO<sup>+</sup>, CH<sub>3</sub>OH, and HNC), including the first detection of three molecules (CN, CH<sub>3</sub>OH, and HNC) in the nuclear region of NGC 4038. The observed spectra at the strongest peak of CO (3–2) are shown in Figure 1 (right). The peak flux density and integrated line intensity of each line are summarized in Table 1. In addition, the 3 mm continuum emission was detected. The integrated intensity maps of five molecular lines and the 3 mm continuum map overlaid on the CO (3–2) integrated intensity map are shown in Figure 2. The integrated intensity maps were made by smoothing and clipping the inten-

sities using the AIPS task, MOMNT. The cleaned image cube was smoothed both spatially and in velocity, and then this cube was clipped at the  $1.5\sigma$  level per channel.

### 3.1 The first detections: CH<sub>3</sub>OH, HNC, and CN

The tracers of shocked gas, CH<sub>3</sub>OH ( $2_k-1_k$ ) and HNC ( $4_{0,4}-3_{0,3}$ ) were detected for the first time. The blended CH<sub>3</sub>OH ( $2_k-1_k$ ) line is composed of three transitions, ( $2_{-1}-1_{-1}$ ) *E*, ( $2_0-1_0$ ) A<sup>+</sup>, and ( $2_0-1_0$ ) *E*. The frequency separations between the two neighbor transition lines are less than 3.2 MHz, which corresponds to  $\lesssim 10$  km s<sup>-1</sup>. Since the velocity resolution of the channel map that we made is 10 km s<sup>-1</sup>, the emission of these transitions cannot be distinguished. Both the CH<sub>3</sub>OH ( $2_k-1_k$ ) and HNC (4–3) emission are distributed around the strongest CO (3–2) peak, and the spatial distribution of the HNC (4–3) is more compact than that of the CH<sub>3</sub>OH ( $2_k-1_k$ ) (Figure 2). The frequency coverage of our data includes another shock tracer, SiO (2–1), but the SiO (2–1) emission was not detected. The  $3\sigma$  upper limit of the flux density is 5.4 mJy beam<sup>-1</sup> ( $\theta_{\text{beam}} = 1''.00 \times 0''.65$ ). Assuming that the line width of the SiO is the same as the HNC line width (53 km s<sup>-1</sup>), the  $3\sigma$  upper limit of the integrated intensity is estimated to be 0.30 Jy km s<sup>-1</sup>.

Two transitions of CN were also detected for the first time. One transition is the CN (1–0; 3/2–1/2) line which is composed of five hyperfine lines, and the other is the CN (1–0; 1/2–1/2) line which is composed of four hyperfine lines. The CN (1–0; 3/2–1/2)/CN (1–0; 1/2–1/2) peak intensity ratio is  $2.2 \pm 0.2$ , which is consistent with the statistical value within the uncertainties, suggesting that the CN (1–0; 1/2–1/2) line is optically thin. Since the CN (1–0; 1/2–1/2) emission is very faint, we use the CN (1–0; 3/2–1/2) (hereafter CN (1–0)) map in the following discussion.

### 3.2 The HCN and HCO<sup>+</sup> emission

The HCN (1–0) and HCO<sup>+</sup>(1–0) emission was clearly detected in the central 1 kpc region. Both emission are concentrated in a region associated with the strongest CO (3–2) peak, but the HCN and HCO<sup>+</sup> peaks are offset by  $0''.4$ . The HCN and HCO<sup>+</sup> integrated intensities are 82% and 89% of previous measurements with ALMA (Schirm et al. 2016), respectively. These differences are due to the limited maximum recoverable scale (MRS). The MRS of our data is 1.3 kpc, which is 2.7 times smaller than the MRS of the previous data (Schirm et al. 2016). We estimate the HCN (1–0)/HCO<sup>+</sup>(1–0) line ratio using the integrated intensity maps clipped at  $2\sigma$  levels. We ignore a slight ( $0''.01$ ) difference between the beam sizes of the HCN and HCO<sup>+</sup> maps. The average luminosity ratio of  $L_{\text{HCN}}/L_{\text{HCO}^+}$  is  $1.2 \pm 0.9$ . The standard deviation quoted reflects the distribution of the HCN/HCO<sup>+</sup> luminosity ratios (the uncertainty based on the calibration uncertainties is  $1.2 \pm 0.1$ ). This av-

erage ratio is 1.2 times higher than the previous measurement ( $L_{\text{HCN}}/L_{\text{HCO}^+} = 1.019 \pm 0.008$ ; Schirm et al. 2016). This difference could be affected by the difference of the MRS and clipping. The variation of the line ratios may show differences of abundances and excitation, and additional data are required to confirm the causes of the various line ratios.

### 3.3 The 3 mm Continuum emission

The total flux of the 3 mm continuum estimated by integrating the extended emission is  $0.59 \pm 0.03$  mJy. The 3 mm continuum peak is located  $\sim 1''$  (100 pc) south of the strongest CO (3–2) peak and corresponds to the 6 cm and 4 cm continuum sources. In order to estimate the radio spectral index with beam-matched radio maps, we reimaged the 6 cm and 4 cm continuum emission using the VLA archival calibrated data (PI: A. Pedlar) obtained with A and B configurations. We clipped the visibilities so that the VLA and ALMA data have the same shortest uv range (9.7 k $\lambda$ ) and convolved both data to  $1''.2$  angular resolution. The peak flux of the 6 cm and 4 cm continuum are  $0.94 \pm 0.07$  mJy and  $0.84 \pm 0.09$  mJy, respectively. The radio spectral index is estimated to be  $\alpha = -0.18 \pm 0.34$ , indicating that the 6 cm and 4 cm continuum emission is dominated by free-free emission from ionized gas. Using this radio spectral index, the continuum flux at 3 mm is estimated to be  $0.55 \pm 0.24$  mJy. This is consistent with the observed value within the error. Thus the 3 mm continuum emission is dominated by free-free emission.

## 4 Discussion

The following discussion in §4.1–§4.3 are based on maps which were created with visibilities clipped to have similar shortest uv range (uv distance = 12–14 k $\lambda$ ), and convolved to  $1''.2$  angular resolution. The maps are not sensitive to extended ( $> 1.0$  kpc) structures.

### 4.1 Photo-Dominated Region

The CN molecule is another tracer of dense gas, with a lower (by a factor of five) critical density than the HCN (Aalto et al. 2002), and the CN/HCN line ratio has been considered to be a tracer of dense Photo-Dominated Regions (PDRs; e.g., Fuente et al. 1993; Boger & Sternberg 2005). It is known that the CN/HCN line ratio increases with the strength of interstellar UV radiation field. We made the CN (1–0)/HCN (1–0) line ratio map (Figure 3) using the convolved CN (1–0) and HCN (1–0) integrated intensity maps clipped at the  $2\sigma$  levels. Although the average ratio (CN/HCN =  $0.7 \pm 0.3$ ) is lower than the global CN (1–0)/HCN (1–0) line ratios measured in typical starburst galaxies (e.g., Arp 220 and NGC 253; Baan et al. 2008), we find a gradient in the CN/HCN line ratio. The enhanced CN/HCN line ratios ( $\simeq 0.8$ – $1.2$ ) are seen in the south-

ern region of the strongest CO (3–2) peak (Figure 3), where the 3 mm continuum peak is also located. Although the resolution of the *Spitzer*/MIPS 24  $\mu\text{m}$  image is  $6''$ , which is five times lower than the resolutions of the convolved CN and HCN maps, the 24  $\mu\text{m}$  peak is located 200 pc south of the strongest CO (3–2) peak, and roughly corresponds to the region associated with high CN/HCN line ratios. Thus, the enhanced CN/HCN line ratios suggest the presence of PDRs.

It is also known that the  $\text{C}_2\text{H}$  emission is enhanced in PDRs (e.g., Fuente et al. 1993). Although the frequency coverage of our data included the set of the  $\text{C}_2\text{H}$  (1–0) lines whose rest frequencies are around 87.4 GHz, the emission was not detected. The  $3\sigma$  upper limit of the flux density is  $5.4 \text{ mJy beam}^{-1}$ . From spectra obtained by Fuente et al. (2005), the  $\text{C}_2\text{H}$  (1–0)/HCN (1–0) peak intensity ratios are estimated to be 0.2–0.4 in the central 650 pc disk in M82 where PDRs form. Assuming the same  $\text{C}_2\text{H}$ /HCN line ratios, the  $\text{C}_2\text{H}$  peak flux density is expected to be  $\leq 3.0 \text{ mJy beam}^{-1}$  for regions in NGC 4038 where the CN/HCN line ratios are larger than 0.8. This expected peak flux density is smaller than the  $3\sigma$  upper limit. New maps with higher sensitivity are required to investigate the properties of the  $\text{C}_2\text{H}$  molecules in the central region of NGC 4038.

## 4.2 Dense gas fraction

We investigate the dense gas fraction in the central region of NGC 4038. Bigiel et al. (2015) estimate the dense gas fraction in the Antennae galaxies using low-resolution ( $\theta_{\text{beam}} = 6''.5$ ) HCN (1–0) and CO (1–0) maps. The dense gas fraction is estimated to be  $\sim 11\%$  in the central  $\sim 700$  pc region of NGC 4038 (Region ID = 1; Bigiel et al. 2015). Schirm et al. (2016) estimate the HCN (1–0)/CO (1–0) line ratio using the HCN (1–0) and CO (1–0) maps with angular resolutions of  $\sim 4''$ , though they do not convert the line ratio into the dense gas fraction. Since a high-resolution ( $\leq 4''$ ) CO (1–0) map is not currently available, we estimate the dense gas fraction from the HCN (1–0)/CO (3–2) line ratio, assuming a single CO (3–2)/CO (1–0) line ratio. Although CO (3–2) is not the best tracer of diffuse molecular gas, the critical density of CO (3–2) is two orders of magnitude lower than that of the HCN (1–0). The resolution of the CO (3–2) SV data is comparable to that of the new HCN (1–0) data, and these data allow us to compare the gas distributions at a 100 pc scale. The luminosity ratios of  $L_{\text{HCN}}/L_{\text{CO (3–2)}}$  range from 0.01 to 0.34, suggesting that the dense gas fraction vary within the central 1 kpc. One peak of the line ratio is located on the northwest side of the strongest HCN (1–0) peak, and the other peaks are found at the south end of the HCN distribution and at the HCN peak located in the middle of the HCN distribution. We convert the HCN (1–0)/CO (3–2) line ratios into HCN (1–0)/CO (1–0) line ratios, assuming the CO (3–2)/(1–0) line ratio of 0.6, which was measured using the CO (1–0) and

CO (3–2) maps of NGC 4038 with  $\sim 4''.6$  resolution (Ueda et al. 2012). The average luminosity ratio of  $L_{\text{HCN}}/L_{\text{CO (1–0)}}$  is  $0.08 \pm 0.03$ . This is consistent with a previous study by Schirm et al. (2016) using maps with a resolution of  $\sim 4''$ .

We estimate the dense gas mass fraction ( $M_{\text{HCN}}/M_{\text{H}_2}$ ) using the same conversion factors as the previous study (Bigiel et al. 2015) in order to estimate the dense gas mass fraction under the same assumptions. We use a Galactic CO-to- $\text{H}_2$  mass conversion factor  $\alpha_{\text{CO}} = 4.35 M_{\odot} (\text{K km s}^{-1} \text{ pc}^2)^{-1}$  (e.g., Bolatto et al. 2013) and the HCN-to-dense gas mass conversion factor  $\alpha_{\text{HCN}} = 10 M_{\odot} (\text{K km s}^{-1} \text{ pc}^2)^{-1}$  (Gao & Solomon 2004). The average dense gas fraction is estimated to be  $17\% \pm 8\%$ , which is larger than previously reported ( $\sim 11\%$  measured in ID=1 by Bigiel et al. 2015). This is expected, since the CO (3–2) emission comes from more compact gas cores than extended gas components traced in the CO (1–0). We note that our estimation has a large uncertainty because the dense gas fraction changes depending on the assumed CO (3–2)/CO (1–0) line ratio. Assuming the CO (3–2)/CO (1–0) line ratio of 0.7 and 0.5, the average dense gas fraction changes to  $\sim 20\%$  and  $\sim 14\%$ , respectively. Furthermore, Zhu et al. (2003) propose a conversion factor for the nucleus of NGC 4038 of  $2.3 \times 10^{19} \text{ cm}^{-2} (\text{K km s}^{-1})^{-1}$ , which corresponds to  $\alpha_{\text{CO}} \sim 0.4$ . This is approximately an order of magnitude lower than the Galactic value, and it is also lower than the conversion factor in gas-rich galaxies at high redshift and local luminous infrared galaxies ( $\alpha_{\text{CO}} = 0.6\text{--}0.8$ ; e.g., Papadopoulos et al. 2012). Adapting this conversion factor, the average dense gas fraction exceeds 100%. While this is not plausible, it shows that the dense gas fraction can change significantly depending on the mass conversion factor. Also, the HCN-to-dense gas mass conversion factor may vary and affect the dense gas fraction. These two conversion factors should be investigated in future studies.

## 4.3 Systematic distributions of different molecular species and continuum emission

The flux profiles as a function of the projected distance from the strongest CO (3–2) peak are shown in Figure 4 (left). We measured the integrated intensities of the CN (1–0), HCN (1–0), and CO (3–2), and the 3 mm and 850  $\mu\text{m}$  continuum flux in nine points arranged in the north-south direction, which are roughly located along strong CO (3–2) emission. The separation between the measurement points is  $0''.6$ , which is a half of the convolved beam size. The HCN profile is very similar to the CO profile. The CN profile is slightly different from the HCN and CO profiles and similar to the 850  $\mu\text{m}$  continuum profile. The peak of the CN integrated intensity shifts toward the south compared to the HCN and CO peaks. The 3 mm continuum profile shifts further toward the south. These comparisons reveal the systematic differences in distribution of the different



molecular species and the continuum emission, and in particular, the softening of the interstellar radiation field (as traced by the CN/HCN ratio) as a function of distance from the star forming region. Such systematic differences are found in the supergiant H II region in M33 (Miura et al. 2010). A star forming region identified by the free-free emission at 3 mm is located  $\sim 100$  pc south of the CO peak. The formation of high mass stars is currently taking place at the  $850 \mu\text{m}$  emission peak, and it is located  $\sim 50$  pc south from the CO peak. It is likely that PDRs are forming in these star forming regions because the CN/HCN line ratios are enhanced (CN/HCN  $\simeq 0.8$ – $1.2$ ). The HCN (1–0)/CO (1–0) luminosity ratios estimated from the HCN (1–0) and CO (3–2) maps (§ 4.1) are  $>0.09$  around the CO peak, which are comparable to the HCN (1–0)/CO (1–0) line ratios ( $\sim 0.1$ ) in molecular clouds in the nuclear starburst region of NGC 253 (Leroy et al. 2015). This implies a large concentration of dense gas (the dense gas fraction  $>20\%$ ) around the CO peak in NGC 4038. Furthermore, the molecular gas mass within a  $0''.6$  ( $\sim 60$  pc) radius of the CO peak is estimated to be  $1.1 \times 10^8 M_{\odot}$ , using the CO (3–2)/CO (1–0) line ratio of 0.6 (Ueda et al. 2012) and  $\alpha_{\text{CO}} = 4.35 M_{\odot} (\text{K km s}^{-1} \text{pc}^2)^{-1}$  (Bolatto et al. 2013). The large molecular gas mass and high dense gas fraction may signify intense star formation around the CO peak.

#### 4.4 Different distributions of two shock tracers

The CH<sub>3</sub>OH and HNCO emission in galaxies has been used to trace large-scale molecular shocks (e.g., García-Burillo et al. 2001; Meier & Turner 2005). Using a CH<sub>3</sub>OH map convolved to the beam size of the HNCO map, the CH<sub>3</sub>OH ( $2_k$ – $1_k$ )/HNCO (4–3) peak intensity ratio is  $1.7 \pm 0.1$  in the CH<sub>3</sub>OH emission peak. This is similar to the CH<sub>3</sub>OH (2–1)/HNCO (4–3) ratios measured in other galaxies. The CH<sub>3</sub>OH (2–1)/HNCO (4–3) ratios are 1.4 for the northern arm of IC 342 (Meier & Turner 2005) and 1.5 for the circum-nuclear disk of NGC 1068 (García-Burillo et al. 2010). On the other hand, the peak intensity ratio is  $0.79 \pm 0.06$  in the HNCO emission peak, which is about half of the ratio in the CH<sub>3</sub>OH emission peak. Furthermore, the distribution of the HNCO emission is different from the CH<sub>3</sub>OH distribution (Figure 3). This could be due to the stellar UV field. The HNCO distribution can be affected by strong UV field because the HNCO molecule is easily photodissociated (Martín et al. 2008). Another possibility is that the CH<sub>3</sub>OH is enhanced by UV field because of desorption into gas-phase from dust by UV photons (Guzmán et al. 2013). As shown in Figure 3, the CH<sub>3</sub>OH distribution is more extended than the HNCO, and the CH<sub>3</sub>OH emission is detected in a region associated with high ( $\geq 0.8$ ) CN/HCN line ratios. The flux profiles (Figure 4 (right)) also show that the HNCO emission is diminished around the CN peak compared to the CH<sub>3</sub>OH emission. Since the CN/HCN line ratio is a tracer of dense PDR, the

different distributions of CH<sub>3</sub>OH and HNCO could be caused by the stellar UV field.

#### 4.5 Possibilities of the shock origin

One possibility of the shock origin is collisions between inflowing gas and a massive molecular complex. We applied the automatic clump identification algorithm Clumpfind (Williams et al. 1994) to the ALMA CO (3–2) SV data, using the recommended  $2\sigma$  threshold to identify robust molecular clumps. The most massive molecular complex (Complex 1) is identified in a region associated with the strongest CO (3–2) peak (Figure 5). The radius and systemic velocity of Complex 1 are  $144 \pm 30$  pc and  $1620 \text{ km s}^{-1}$ , respectively. The molecular gas mass of Complex 1 is estimated to be  $3.2 \times 10^8 M_{\odot}$ , using the CO (3–2)/CO (1–0) line ratio of 0.6 (Ueda et al. 2012) and  $\alpha_{\text{CO}} = 4.35 M_{\odot} (\text{K km s}^{-1} \text{pc}^2)^{-1}$  (Bolatto et al. 2013). The molecular gas indicated by blue cross symbols in Figure 5 moves toward Complex 1 and merges with Complex 1 as the velocity goes from  $1600 \text{ km s}^{-1}$  to  $1650 \text{ km s}^{-1}$ . This component appears to inflow toward Complex 1 because the line-of-sight velocity of the gas component is different from a velocity expected from the galactic rotation of NGC 4038. According to the velocity fields of atomic gas (Hibbard et al. 2001) and ionized gas (Amram et al. 1992), NGC 4038 has a single trailing arm extending toward the southwest. The southwest part of this galaxy is located on the front side, and the northeast part is located on the rear side. Based on this geometry, the line-of-sight velocities of molecular gas distributed along the arm should decrease as closer to the center (i.e., Complex 1). However, the line-of-sight velocities of the gas indicated by blue cross symbols in Figure 5 increase as closer to Complex 1. We thus suggest that the gas component is inflowing toward Complex 1. We note that we cannot completely reject other possibilities (e.g., outflow) because the structure and velocity field in the central region are significantly disturbed and complicated due to the dynamical interaction. The shocked gas traced in the CH<sub>3</sub>OH and HNCO emission is seen around a region where the inflowing gas component connects with Complex 1, and the line-of-sight velocities of the shocked gas are consistent with those of the inflowing gas component and Complex 1. Therefore, we suggest that the CH<sub>3</sub>OH and HNCO emission traces molecular shocks caused by collisions between the inflowing gas and the central massive molecular complex.

Another possibility of the shock origin is outflows induced by star formation, as often demonstrated in Galactic sources. A typical size of shock regions created by star formation is  $\sim 0.1$ – $1$  pc (e.g., L1157; Gueth et al. 1998), but the shocked gas is distributed across a few 100 pc in the nuclear region of NGC 4038. Such a large-scale shock can be caused by a kinematic factor rather than by star formation. It is likely that the emis-

sion of the shock tracers comes from multiple sites of cloud-cloud collisions. In addition, we estimate the number density of outflows which would be required to reproduce the observed CH<sub>3</sub>OH intensity in the nuclear region of NGC 4038, using the CH<sub>3</sub>OH luminosity measured in the blue lobe of L1157. The same discussion has been conducted using the SiO emission by Usero et al. (2006). The mean CH<sub>3</sub>OH intensity in NGC 4038 is 5.55 mJy km s<sup>-1</sup>, which corresponds to 1.60 K km s<sup>-1</sup>. According to Usero et al. (2006), the CH<sub>3</sub>OH luminosity is 0.50 K km s<sup>-1</sup> pc<sup>2</sup> in the blue lobe of L1157. Thus the required number density of outflows is estimated to be 3.2 outflows pc<sup>-2</sup>. Although star-forming regions with a few outflows pc<sup>-2</sup> are found (e.g., Williams et al. 2003), it is unlikely that such star-forming regions is forming across a few 100 pc<sup>2</sup>. This is the same conclusion as the previous study towards IC 342 (Usero et al. 2006).

Finally, we discuss shock strength using the CH<sub>3</sub>OH/SiO and HNCO/SiO line ratios. The CH<sub>3</sub>OH/SiO line ratio is used as an indicator of shock strength because the CH<sub>3</sub>OH molecules could be destroyed by relatively slow shocks ( $v_{\text{shock}} > 10\text{--}15$  km s<sup>-1</sup>) and the dissociation of the SiO molecules would require fast shocks ( $v_{\text{shock}} > 50\text{--}60$  km s<sup>-1</sup>) (Usero et al. 2006). The HNCO/SiO line ratio can be also an indicator of shock strength because the HNCO molecules could be sublimated by weak shocks (Rodríguez-Fernández et al. 2010; Meier et al. 2015). We estimate the lower limits of the CH<sub>3</sub>OH/SiO and HNCO/SiO line ratios in the nuclear region of NGC 4038, using the 3 $\sigma$  upper limit of the SiO flux density (5.4 mJy beam<sup>-1</sup>). The lower limits of the CH<sub>3</sub>OH/SiO and HNCO/SiO peak intensity ratios are 2.0 and 1.9, respectively. These are comparable to the line ratios measured in both the young bipolar outflow L1157 and the circum-nuclear disk of NGC 1068 (García-Burillo et al. 2010). This suggests that fast shocks may have occurred in the nuclear region of NGC 4038. However, if the SiO emission is much weaker than the 3 $\sigma$  upper limit, the line ratios become larger, indicating that a possibility for the presence of fast shocks is reduced. High-sensitivity SiO measurements are required to draw a conclusion about the shock strength in the nuclear region of NGC 4038.

## 5 Summary

We have conducted multi-line observations ( $\lambda = 3$  mm) of NGC 4038 using ALMA. Five molecules (CN, HCN, HCO<sup>+</sup>, CH<sub>3</sub>OH, and HNCO) were detected in the central  $\leq 1$  kpc region, and three (CN, CH<sub>3</sub>OH, and HNCO) of them was detected for the first time in this region.

The flux profiles as a function of the distance from the CO (3–2) peak reveal the systematic differences in distributions of the different molecular species and continuum emission. A star forming region identified by the free-free emission (the

3 mm continuum emission) and the most active site of dusty star forming region (the 850  $\mu$ m continuum emission) are located  $\sim 100$  pc and  $\sim 50$  pc, respectively, south of the HCN (1–0) and CO (3–2) peaks. The CN (1–0)/HCN (1–0) line ratios are enhanced (CN/HCN  $\simeq 0.8\text{--}1.2$ ) in these star forming regions, suggesting the presence of PDRs. Assuming the CO (3–2)/CO (1–0) line ratio of 0.6, the average HCN (1–0)/CO (1–0) luminosity ratio is estimated to be  $0.08 \pm 0.03$ . This corresponds to the dense gas fraction of  $17\% \pm 8\%$ . The large molecular gas mass ( $10^8 M_{\odot}$ ) and high dense gas fraction ( $>20\%$ ) are found around the CO peak, which suggests potential star formation there.

The detection of the shocked gas traced in the CH<sub>3</sub>OH and HNCO emission is evidence for sub-kpc scale molecular shocks. The distribution of the HNCO is slightly different from the CH<sub>3</sub>OH distribution. The CH<sub>3</sub>OH emission is detected in a region associated with high ( $\geq 0.8$ ) CN/HCN line ratios. Since the CN/HCN line ratio is a tracer of PDR, the different distributions of CH<sub>3</sub>OH and HNCO could be caused by the stellar UV field. Comparing the distributions of the shocked gas and the CO (3–2) emission, we suggest that the molecular shocks could be caused by collision between inflowing gas and the central massive molecular complex.

## Acknowledgments

This paper has made use of the following ALMA data: ADS/JAO.ALMA#2012.0.01000.S and ALMA Science Verification data: ADS/JAO.ALMA#2011.0.00003.SV. ALMA is a partnership of the ESO (representing its member states), NSF (USA), and NINS (Japan), together with the NRC (Canada), NSC, and ASIAA (Taiwan), in cooperation with the Republic of Chile. The Joint ALMA Observatory is operated by the ESO, AUI/NRAO, and NAOJ.

One image presented in this paper were obtained from the Mikulski Archive for Space Telescopes (MAST). STScI is operated by the Association of Universities for Research in Astronomy, Inc., under NASA contract NAS5-26555. Support for MAST for non-HST data is provided by the NASA Office of Space Science via grant NNX09AF08G and by other grants and contracts.

Data analysis were in part carried out on common use data analysis computer system at the Astronomy Data Center, ADC, of the National Astronomical Observatory of Japan.

J.U. was supported by the ALMA Japan Research Grant of NAOJ Chile Observatory, NAOJ-ALMA-0058. S.O. and T.S. are financially supported by a Research Fellowship from the Japan Society for the Promotion of Science for Young Scientists.

## References

- Aalto, S., Polatidis, A. G., Hüttemeister, S., & Curran, S. J. 2002, *A&A*, 381, 783
- Amram, P., Marcelin, M., Boulesteix, J., & Le Coarer, E. 1992, *A&A*, 266, 106
- Baan, W. A., Henkel, C., Loenen, A. F., Baudry, A., & Wiklind, T. 2008, *A&A*, 477, 747
- Bigiel, F., Leroy, A. K., Blitz, L., et al. 2015, *ApJ*, 815, 103

- Bolatto, A. D., Wolfire, M., & Leroy, A. K. 2013, *ARA&A*, 51, 207
- Boger, G. I., & Sternberg, A. 2005, *ApJ*, 632, 302
- Fuente, A., García-Burillo, S., Gerin, M., et al. 2005, *ApJL*, 619, L155
- Fuente, A., Martín-Pintado, J., Cernicharo, J., & Bachiller, R. 1993, *A&A*, 276, 473
- Gao, Y., & Solomon, P. M. 2004, *ApJS*, 152, 63
- García-Burillo, S., Martín-Pintado, J., Fuente, A., & Neri, R. 2001, *ApJL*, 563, L27
- García-Burillo, S., Usero, A., Fuente, A., et al. 2010, *A&A*, 519, A2
- Gueth, F., Guilloteau, S., & Bachiller, R. 1998, *A&A*, 333, 287
- Guzmán, V. V., Goicoechea, J. R., Pety, J., et al. 2013, *A&A*, 560, A73
- Hibbard, J. E., van der Hulst, J. M., Barnes, J. E., & Rich, R. M. 2001, *AJ*, 122, 2969
- Hibbard, J. E., & van Gorkom, J. H. 1996, *AJ*, 111, 655
- Iono, D., Yun, M. S., & Ho, P. T. P. 2005, *ApJS*, 158, 1
- Kewley, L. J., Rupke, D., Zahid, H. J., Geller, M. J., & Barton, E. J. 2010, *ApJL*, 721, L48
- Klaas, U., Nielbock, M., Haas, M., Krause, O., & Schreiber, J. 2010, *A&A*, 518, L44
- Leroy, A. K., Bolatto, A. D., Ostriker, E. C., et al. 2015, *ApJ*, 801, 25
- Lundgren, A. 2013, *ALMA Cycle 2 Technical Handbook Version 1.1*, ALMA
- Martín, S., Requena-Torres, M. A., Martín-Pintado, J., & Mauersberger, R. 2008, *ApJ*, 678, 245-254
- McElroy, D., Walsh, C., Markwick, A. J., et al. 2013, *A&A*, 550, A36
- Meier, D. S., & Turner, J. L. 2005, *ApJ*, 618, 259
- Meier, D. S., Walter, F., Bolatto, A. D., et al. 2015, *ApJ*, 801, 63
- Mihos, J. C., & Hernquist, L. 1996, *ApJ*, 464, 641
- Miura, R., Okumura, S. K., Tosaki, T., et al. 2010, *ApJ*, 724, 1120
- Papadopoulos, P. P., van der Werf, P., Xilouris, E., Isaak, K. G., & Gao, Y. 2012, *ApJ*, 751, 10
- Rampazzo, R., Plana, H., Amram, P., et al. 2005, *MNRAS*, 356, 1177
- Rodríguez-Fernández, N. J., Tafalla, M., Gueth, F., & Bachiller, R. 2010, *A&A*, 516, A98
- Schirm, M. R. P., Wilson, C. D., Madden, S. C., & Clements, D. L. 2016, *ApJ*, 823, 87
- Schulz, A., Henkel, C., Muders, D., Mao, R. Q., Röllig, M., & Mauersberger, R. 2007, *A&A*, 466, 467
- Schweizer, F., et al. 2008, *AJ*, 136, 1482
- Teyssier, R., Chapon, D., & Bournaud, F. 2010, *ApJL*, 720, L149
- Ueda, J., Iono, D., Petitpas, G., et al. 2012, *ApJ*, 745, 65
- Usero, A., García-Burillo, S., Martín-Pintado, J., Fuente, A., & Neri, R. 2006, *A&A*, 448, 457
- Wang, Z., Fazio, G. G., Ashby, M. L. N., et al. 2004, *ApJS*, 154, 193
- Whitmore, B. C., Brogan, C., Chandar, R., et al. 2014, *ApJ*, 795, 156
- Williams, J. P., de Geus, E. J., & Blitz, L. 1994, *ApJ*, 428, 693
- Williams, J. P., Plambeck, R. L., & Heyer, M. H. 2003, *ApJ*, 591, 1025
- Wilson, C. D., Scoville, N., Madden, S. C., & Charmandaris, V. 2000, *ApJ*, 542, 120
- Zhu, M., Seaquist, E. R., & Kuno, N. 2003, *ApJ*, 588, 243

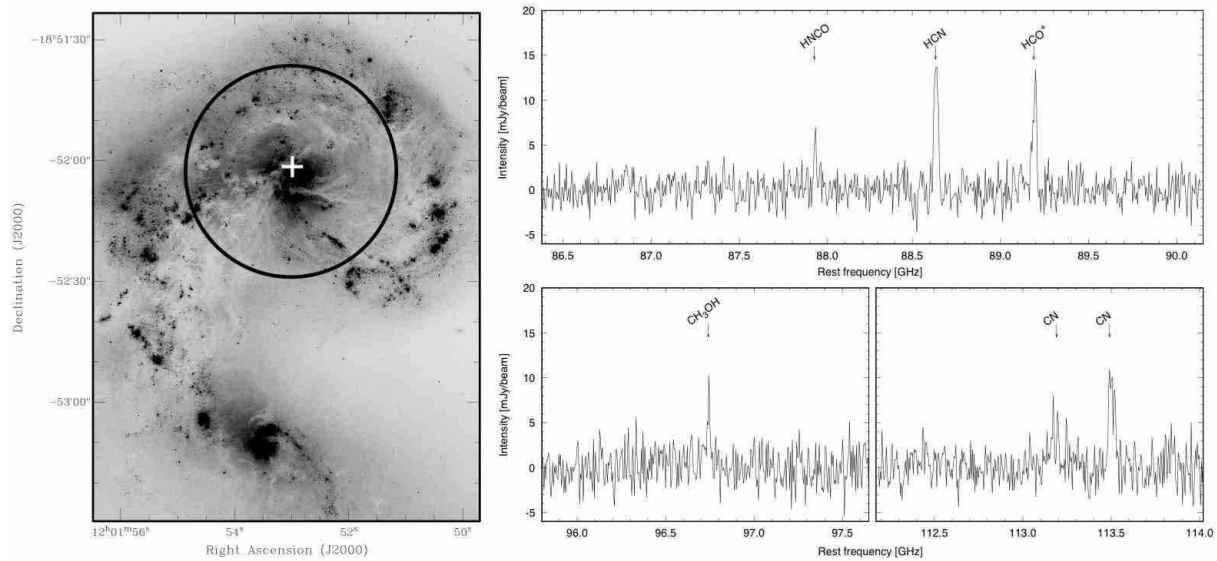


**Fig. 1.** (left) The *HST*/WFC3 F625W image of the Antennae galaxies. The black circle shows the primary beam of the ALMA 12 m antenna. (right) The observed spectra at the strongest CO (3–2) peak shown by a white cross in the left figure. The frequency resolution is 4.88 MHz.

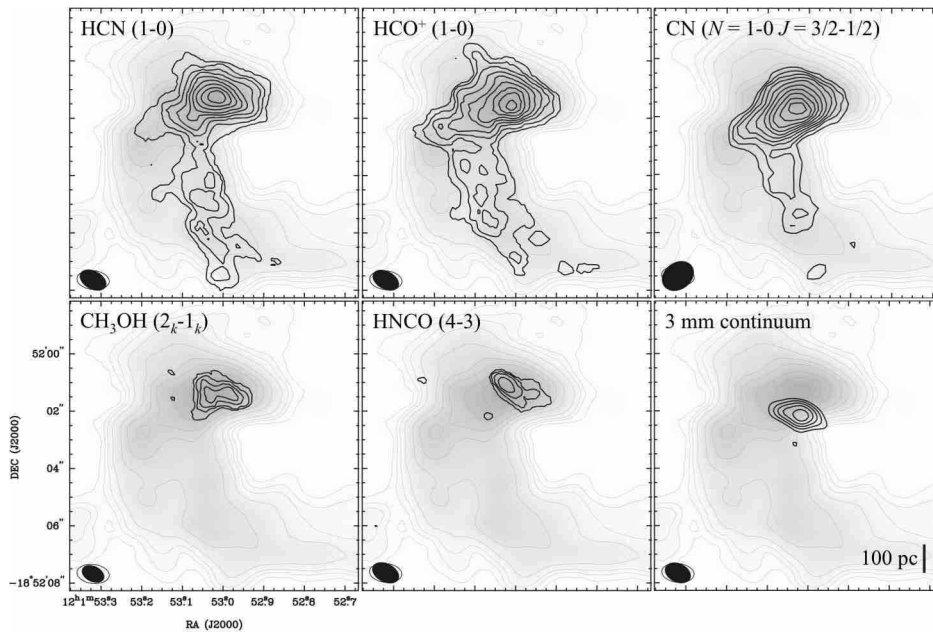


**Fig. 2.** Integrated intensity contour maps of five molecular lines and the 3mm continuum map. The background image with gray contours is the CO (3–2) integrated intensity map. The filled and open ellipses in the bottom-left corner show the beam sizes of the new map and the CO (3–2) map, respectively. The length of each side corresponds to  $10''$  ( $\sim 1.1$  kpc). Contour levels are  $120 \text{ mJy beam}^{-1} \text{ km s}^{-1} \times n$  for the HCN map,  $110 \text{ mJy beam}^{-1} \text{ km s}^{-1} \times n$  for the HCO<sup>+</sup> map,  $110 \text{ mJy beam}^{-1} \text{ km s}^{-1} \times n$  for the CN map,  $90 \text{ mJy beam}^{-1} \text{ km s}^{-1} \times n$  for the CH<sub>3</sub>OH map,  $65 \text{ mJy beam}^{-1} \text{ km s}^{-1} \times n$  for the HNCO map ( $n = 1, 2, 3, \dots$ ). Contour levels are  $50 \text{ mJy beam}^{-1} \times (3, 4, 5, 6, 7)$  for the 3 mm continuum map and  $2 \text{ Jy beam}^{-1} \text{ km s}^{-1} \times (1, 2, 3, 5, 10, 15, 20, 30, 40, 50)$  for the CO map. The integrated velocity ranges are  $250 \text{ km s}^{-1}$  ( $1500\text{--}1750 \text{ km s}^{-1}$ ) for the HCN, HCO<sup>+</sup>, CN, and CO maps,  $100 \text{ km s}^{-1}$  ( $1600\text{--}1700 \text{ km s}^{-1}$ ) for the CH<sub>3</sub>OH map, and  $100 \text{ km s}^{-1}$  ( $1590\text{--}1690 \text{ km s}^{-1}$ ) for the HNCO map.



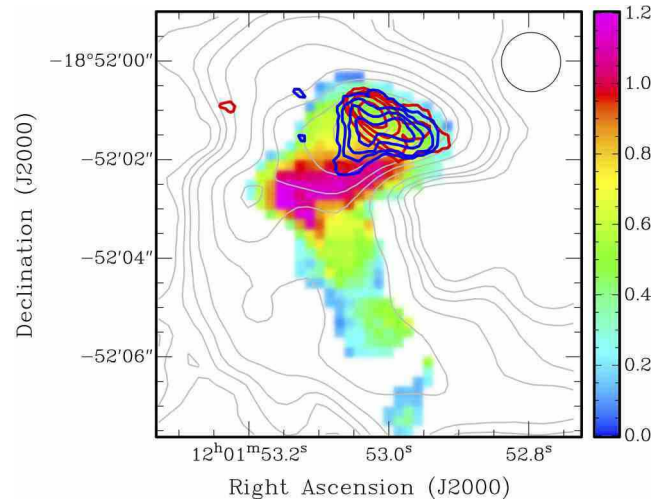


**Fig. 3.** The color-scale image is the CN (1-0; 3/2-1/2)/HCN (1-0) integrated intensity ratio map with a resolution of  $1''.2$  (shown in the upper-right corner). The blue, red, and gray contours show the  $\text{CH}_3\text{OH}$  ( $2_k-1_k$ ), HNCO (4-3), and CO (3-2) integrated intensity maps, respectively. The contour levels are the same as Figure 2.

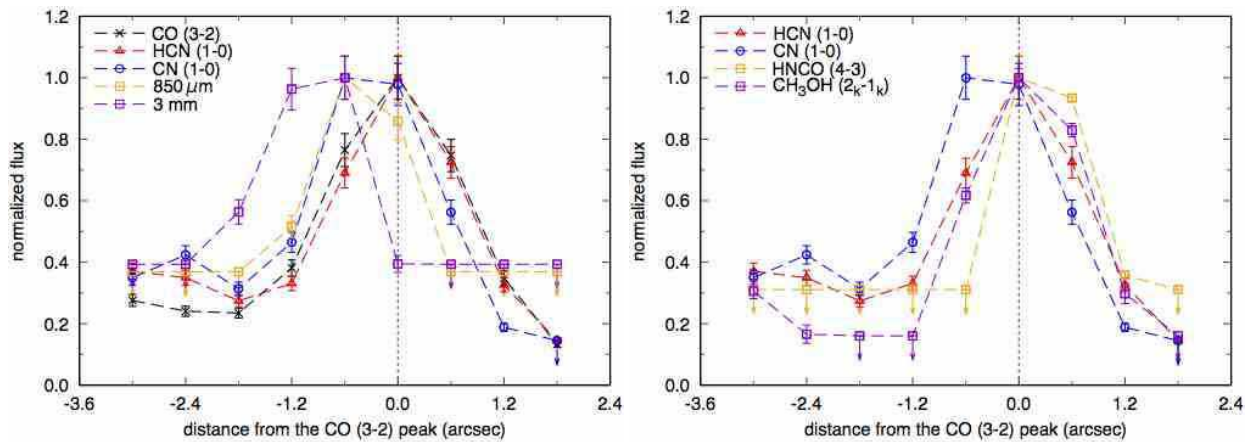


**Fig. 4.** (left) Flux profiles of the CO (3-2), HCN (1-0), CN (1-0),  $850\ \mu\text{m}$  continuum, and 3 mm continuum emission as a function of the projected distance from the strongest CO (3-2) peak. The positive and negative values correspond to the north and south directions. (right) Same as the left figure, but for the HCN (1-0), CN (1-0), HNCO (4-3), and  $\text{CH}_3\text{OH}$  ( $2_k-1_k$ ) lines.

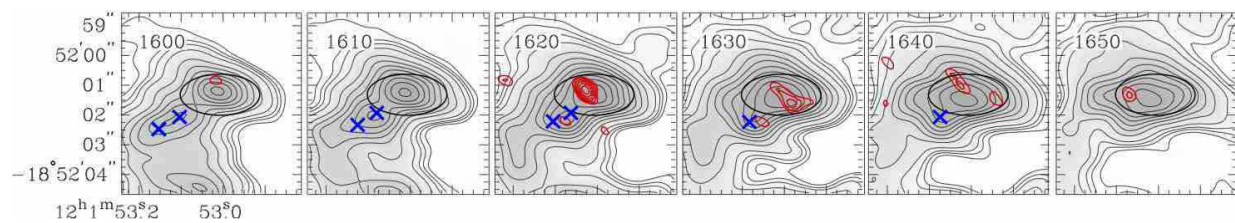


**Fig. 5.** The gray-scale image with black contours is the CO (3-2) channel map with the velocity resolution of  $10\ \text{km s}^{-1}$  in the central  $\sim 300\ \text{pc}$  region. The contour levels are  $23.5\ \text{mJy beam}^{-1} \times (1, 2, 3, 5, 10, 15, 20, 25, 30, 35, 40, 45, 50)$ . The red contours ( $1.8\ \text{mJy beam}^{-1} \times (3.0, 3.5, 4.0, 4.5, 5.0, 5.5)$ ) show the HNCO (4-3) channel map. The black ellipse roughly shows the location of Complex 1 and the blue cross symbols show the inflowing gas (see §4.5).

**Table 1.** Properties of ALMA data for the detected molecular lines

Molecule	Transition	Frequency [GHz]	Beam Size [arcsec]	P.A. [degree]	rms* [mJy Beam <sup>-1</sup> ]	Peak flux density [mJy beam <sup>-1</sup> ]	Integrated intensity [Jy km s <sup>-1</sup> ]
HNCO	4 <sub>0,4</sub> -3 <sub>0,3</sub>	87.925	1.00 × 0.65	62.8	1.8	10.5 ± 0.5	0.66 ± 0.03
HCN	<i>J</i> = 1-0	88.632	1.00 × 0.64	61.7	1.9	15.4 ± 0.8	11.7 ± 0.6
HCO <sup>+</sup>	<i>J</i> = 1-0	89.189	0.99 × 0.63	61.8	1.8	14.5 ± 0.7	12.8 ± 0.6
CH <sub>3</sub> OH	2 <sub><i>k</i></sub> -1 <sub><i>k</i></sub>	96.741	0.83 × 0.55	64.4	2.3	10.8 ± 0.5	1.74 ± 0.09
CN	<i>N</i> = 1-0 <i>J</i> = 1/2-1/2	113.191	1.19 × 0.93	126.4	2.0	8.4 ± 0.4	1.0 ± 0.1
CN	<i>N</i> = 1-0 <i>J</i> = 3/2-1/2	113.491	1.19 × 0.93	126.4	2.1	18.5 ± 0.9	5.7 ± 0.3

\* The noise level in the velocity resolution of 10 km s<sup>-1</sup>.